

Taylor–Couette flow with an imposed magnetic field — linear and nonlinear results

Wolfgang Dobler[†]

Kiepenheuer-Institut für Sonnenphysik, Schöneckstr. 6, D-79104 Freiburg, Germany
New address: *Department of Physics and Astronomy, University of Calgary, 2500 University Drive NW, Calgary AB T2N 1N4, Canada*

Abstract. Using numerical simulations we investigate the (in)-stability and saturation behaviour of moderately compressible, cylindrical Taylor–Couette flow in the presence of a uniform axial magnetic field. For Rayleigh-stable configurations, we find magnetically induced Taylor vortices as predicted by linear theory, with both axisymmetric and non-axisymmetric solutions, depending on the Hartmann number.

The flow shows clear indications of the magneto-rotational instability which is well-known from numerical simulations in accretion disc geometry. In the saturated state, the structure of the flow and the magnetic field can be very different from the linear phase of the instability.

1. TAYLOR–COUETTE FLOW

Taylor–Couette flow — the viscous flow between two rotating coaxial cylinders is — one of the most intensively studied flows in hydrodynamics [for a comprehensive overview, see 1]. For a fluid of constant dynamic viscosity, the Navier–Stokes equation has a simple and highly symmetric solution, the so-called (cylindrical) Couette flow,

$$\omega(r) \equiv \frac{u_\varphi(r)}{r} = \frac{\Omega_2 R_2^2 - \Omega_1 R_1^2}{R_2^2 - R_1^2} - \frac{(\Omega_2 - \Omega_1) R_1^2 R_2^2}{R_2^2 - R_1^2} \frac{1}{r^2}, \quad (1)$$

where R_1 and R_2 denote the radius of the inner and outer cylinder, Ω_1 and Ω_2 are the corresponding angular velocities, and r denotes cylindrical radius. The other two velocity components vanish for Couette flow,

$$u_r = u_z = 0. \quad (2)$$

In the limit of vanishing viscosity, the solution (1), (2) is unstable whenever the specific angular momentum $l_1 \equiv \Omega_1 R_1^2$, $l_2 \equiv \Omega_2 R_2^2$ at the two cylinders satisfies the Rayleigh criterion

$$\text{sgn} \Omega_1 (l_2 - l_1) < 0, \quad (3)$$

(where $\text{sgn} \Omega_1$ denotes the sign of Ω_1) and is stable otherwise. For real fluids, viscosity can damp the instability, and it will only occur if the Taylor number

$$\text{Ta} \equiv \frac{4\Omega_1^2 (R_2 - R_1)^4}{\nu^2} \quad (4)$$

exceeds a certain threshold (ν denotes the kinematic viscosity of the fluid).

If the fluid is electrically well conducting, the presence of a magnetic field can change the stability properties completely [2–5]. The strength of the magnetic field is characterized by a new dimensionless parameter, the Hartmann number

$$\text{Ha} \equiv \frac{B(R_2 - R_1)}{\sqrt{\mu_0 \rho \nu \eta}} = \frac{v_A (R_2 - R_1)}{\sqrt{\nu \eta}}, \quad (5)$$

where μ_0 denotes vacuum permeability, ρ and η density and magnetic diffusivity of the fluid, and $v_A \equiv B/\sqrt{\mu_0 \rho}$ is the Alfvén speed. For an ideal fluid ($\nu = \eta = 0$), the change in stability properties is particularly drastic. For strong magnetic fields or thin gaps $R_2 - R_1$, the magnetic field rather has a stabilizing function [3, 6]. But in the limit of weak magnetic fields, the Couette flow becomes unstable provided that the angular velocities of the two cylinders satisfy the condition

$$\text{sgn} \Omega_1 (\Omega_2 - \Omega_1) < 0, \quad (6)$$

which is much weaker than the Rayleigh criterion (3). This change can be interpreted in terms of the dominant mechanism of angular momentum transport: In the nonmagnetic case advection is the only radial transport mechanism, and thus the gradient of specific angular momentum l (i. e. the deviation from the state $l = \text{const}$ where no angular momentum would be transported) determines the stability of the flow. The magnetic tension force, on the other hand, tries to synchronize angular velocity ω , so in the magnetic case the direction of angular momentum transport is determined by the gradient $d\omega/dr$.

Even as $|\mathbf{B}| \rightarrow 0$, the fastest growth rate is of order $|\Omega_1|$, i. e. remains finite. However, the wave number corresponding to that fastest growing eigenmode scales like $k \sim |\Omega_1|/v_A$, and for very weak magnetic fields, dissipative effects will eventually destroy the instability [see also 7]

This *magnetorotational instability* (MRI), i. e. the destabilizing effect of magnetic fields on rotating shear flows, is thought to be the main mechanism for rendering accretion discs turbulent, and thus viscous. While nonlinear instabilities have been proposed to explain turbulent accretion discs as well [8] and may be relevant for very cool discs, the MRI certainly plays a central role in the theory of accretion discs, and many numerical simulations have confirmed that it is indeed very efficient in transforming a laminar accretion disc into a turbulent one [see e.g. 5, 9–11].

While even weak magnetic fields are enough for the MRI to maintain an accretion disc in a turbulent state, the magnetic fields must eventually be maintained against Ohmic decay. From dynamo theory, we know that magnetic field generation is a natural consequence of the turbulent, three-dimensional nature of the rotating accretion flow. This gives rise to a very elegant scenario for magnetized accretion discs, in which turbulence and magnetic field maintain each other symbiotically. This scenario has been verified in a number of numerical experiments [9, 10, 12].

The importance of the MRI for accretion discs and possibly also for galactic discs [13, 14] is one of the motivations for building magnetic Taylor–Couette laboratory experiments, a topic that will be discussed at length in other chapters of this book. One challenge for experiments is the low electrical conductivity of liquid metals, which makes Ohmic dissipation a much more prominent effect than in astrophysical objects. The low

conductivity also makes it difficult to numerically model laboratory experiments, since the low magnetic Prandtl number ($\text{Pm} \equiv \nu/\eta \sim 10^{-5}$ for liquid sodium and similar or lower for other liquid metals) leads to vastly different scales for the flow and the magnetic field. We believe nevertheless that models with Pm of order unity can teach us a lot about magnetic Taylor–Couette flow. These values make it feasible to conduct parameter studies, and more expensive calculations with lower Pm can be targeted at particularly interesting parameter regimes once these have been identified. Also, highly turbulent media are often modelled with a turbulent magnetic Prandtl number close to unity.

In the context of dissipative magnetic Taylor–Couette flow, the MRI will manifest itself in a modified (lowered) threshold for the formation of Taylor-like vortices, and in the fact that such vortices form for ratios Ω_2/Ω_1 where the Couette profile (1), (2) would be stable in the absence of magnetic fields.

Previous studies have focused on the onset of dynamo action in both the linear [15] and nonlinear case [16]. A related flow, even easier capable of dynamo action, is the so-called helical Couette flow, where the cylinders also move in the axial direction. The resulting velocity field gives rise to the well-known screw dynamo, which is well-investigated both theoretically [17–21] and numerically [22–26].

In the present paper we take a different approach and consider cylindrical Taylor–Couette flow in the presence of an axial, uniform magnetic field $B_0 \mathbf{e}_z$. In this system, magnetic induction due to the imposed field and intrinsic dynamo action cannot easily be disentangled (if at all), but still the resulting flow can have properties that would make it a dynamo in the absence of the external field.

Linear stability analysis of this configuration has shown that the imposed magnetic field indeed gives rise to the MRI as discussed above [27], and for certain parameters, non-axisymmetric Taylor vortices are the preferred modes [28]. These results have been confirmed in the limits of very low and very high magnetic Prandtl number [29].

2. OUR MODEL

2.1. Equations

We consider the flow between two concentric cylinders as described in Sec. 1. Our numerical code uses cylindrical coordinates (r, φ, z) and solves the compressible MHD equations for (logarithmic) density $\ln \rho$, fluid velocity \mathbf{u} , and magnetic vector potential \mathbf{A} ,

$$\frac{D \ln \rho}{Dt} = -\text{div } \mathbf{u}, \quad (7)$$

$$\frac{D \mathbf{u}}{Dt} = -\frac{1}{\rho} \text{grad } p + \frac{\mathbf{j} \times \mathbf{B}}{\rho} + \frac{1}{\rho} \text{div}(2\rho \nu \underline{\underline{S}}), \quad (8)$$

$$\frac{\partial \mathbf{A}}{\partial t} = \mathbf{u} \times \text{curl } \mathbf{A} - \langle (\mathbf{u} \times \mathbf{B}) \cdot \mathbf{e}_r \rangle_{\varphi, z} \mathbf{e}_r + \eta \Delta \mathbf{A}, \quad (9)$$

where $D/Dt \equiv \partial/\partial t + \mathbf{u} \cdot \text{grad}$ denotes the advective time derivative, $\mathbf{B} = \text{curl } \mathbf{A}$ is the magnetic flux density, $\mu_0 \mathbf{j} = \text{curl } \mathbf{B}$ the current density, and $S_{ik} \equiv [\partial_i u_k + \partial_k u_i -$

TABLE 1. Parameters and properties of the different runs. Other parameters are $R_1 = 0.5$, $R_2 = 1$, $L_z = 1$, $\nu = \eta = 7 \times 10^{-4}$. Linear modes are characterized by their axial and azimuthal wave numbers k, m ; longitudinal wave numbers k are listed in units of $2\pi/L_z$. γ denotes the growth rate $d \ln ||u_z||/dt$ of the mode.

Run	Ω_1	Ω_2	B_0	l_2/l_1	Ha	Linear structure	γ	Saturated structure
1a	2.0	0.5	0.00	1.0	0.0	$k = 2, m = 0$	0.13	$k = 2, m = 0$
1b	2.0	0.5	0.02	1.0	14.3	$k = 3, m = 0$	0.48	$k = 3, m = 0$
1c	2.0	0.5	0.05	1.0	35.7	$k = 3, m = 0$	0.72	$k = 3, m = 0$
1d	2.0	0.5	0.10	1.0	71.4	$k = 2$, “wavy”	0.64	$k = 1$, wavy
1e	2.0	0.5	0.20	1.0	142.9	$k = 1, m = 0$	0.42	$k = 1$, wavy
1f	2.0	0.5	0.50	1.0	357.1	$k = 1, m = 0$	-0.03	—
1g	2.0	0.5	1.00	1.0	714.3	$k = 1, m = 0$	-0.03	—
2a	2.0	0.667	0.10	1.33	71.4	$k = 2, m = 1$ “wavy”	0.56	$k = 2$, wavy
3a	2.0	1.0	0.05	2.0	35.7	$k = 3, m = 0$	≈ 0.36	
3b	2.0	1.0	0.10	2.0	71.4	$k = 2, m = 1$	0.36	$k = 2, m = 0$
3c	2.0	1.0	0.20	2.0	142.9	$k = 1$, “wavy”	≈ 0.26	$k = 1$, wavy

$(2/3)\delta_{ik} \text{div } \mathbf{u}] / 2$ is the traceless rate-of-strain tensor. The second term on the right-hand-side of the induction equation (9) does not contribute to the magnetic field and is present for purely numerical reasons. To evolve Eqs. (7)–(9), we use 6th-order finite differences in space and 3rd-order Runge–Kutta time-stepping scheme.

While the code solves the compressible MHD equations (and uses an isothermal equation of state), we think that our results are only moderately influenced by the compressibility of the fluid (but see Sec. 2.3.3 below). For reasons of efficiency, we have used a Mach number of order unity and the corresponding density contrast is about $\rho_2/\rho_1 \approx 1.5$. In other simulations [25], we had found that for a Mach number of about 0.3 weakly compressible and incompressible results are almost identical.

Our initial magnetic field is purely vertical and uniform, $\mathbf{B} = B_0 \mathbf{e}_z$. The initial velocity is the Couette profile (1), (2), superimposed with white noise at very low amplitude.

The vertical boundary conditions are periodic, while radially we have no-slip, impenetrable conditions for the velocity and perfectly conducting conditions for the magnetic field. We note that these magnetic boundary conditions do not allow the total magnetic flux between the cylinders to change and thus our magnetic field has no chance of decaying.

2.2. Parameters

The inner and outer radius are chosen as $R_1 = 0.5$, $R_2 = 1$, while the full height of the (periodic) cylinders is $L_z = 1$. In all runs presented here, viscosity and magnetic permeability are equal, i. e. the magnetic Prandtl number is $\text{Pm} = 1$. Table 1 lists other parameters of the individual runs, together with some of the properties of the flow and magnetic field.

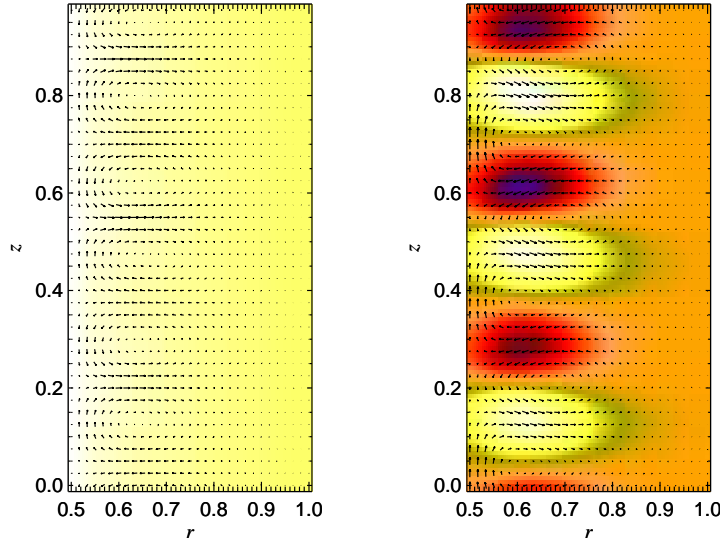


FIGURE 1. Horizontal sections of velocity \mathbf{u} (left) and residual magnetic field $\mathbf{B}_{\text{res}} \equiv \mathbf{B} - B_0 \mathbf{e}_z$ (right) for the linear phase of Run 1b. Arrows indicate the tangential components u_ϕ, u_z , while colours represent the radial component with bright (dark) colours representing a component towards (away from) the viewer, i. e. positive (negative) B_r . [As an exception, the sign has been reversed for u_ϕ , so bright colour means *positive* u_ϕ here to avoid excessive dark colours.] Both velocity and magnetic field are axisymmetric in this run.

2.3. Results

2.3.1. Geometry

As Table 1 shows, varying the Hartmann number changes the structure of the linear modes considerably. For weak magnetic fields (Runs 1b, 1c), the preferred mode has three nodes in the vertical direction, i. e. the vertical size of the cylinder accommodates six Taylor half-cells. This configuration is shown in Fig. 1. With increasing Hartmann number Ha , the vertical wave number gets larger, as the magnetic field is able to synchronize velocity over a larger vertical distance. For both weak and strong magnetic field, the vortices are axisymmetric (azimuthal wave number $m = 0$).

However, for Run 1d with its moderate Hartmann number of about 70, the linear stage shows a “wavy” mode (see below), and the same holds for Run 2a which has the same Hartmann number. The velocity for the latter case is shown in Figure 2, which shows the full velocity and the residual magnetic field $\mathbf{B}_{\text{res}} \equiv \mathbf{B} - B_0 \mathbf{e}_z$, on a cylindrical surface, while Fig. 3 shows the same in a vertical section. One can clearly see the vertical wave number $k = 2k_1$, where $k_1 \equiv 2\pi/L_z$ is the lowest non-vanishing wave number compatible with the vertical size L_z of the cylinder.

The azimuthal structure is a superposition of different wave numbers with at least $m = 0, \pm 1$ prominently present. Note that here during the linear phase these modes evolve independently and must thus have very similar growth rates to coexist for a long time. We note that, from Taylor–Couette experiments, the “wavy mode” is known [1], where nodal surfaces of u_z (or similar diagnostics) are not planar, but oscillate in ϕ .

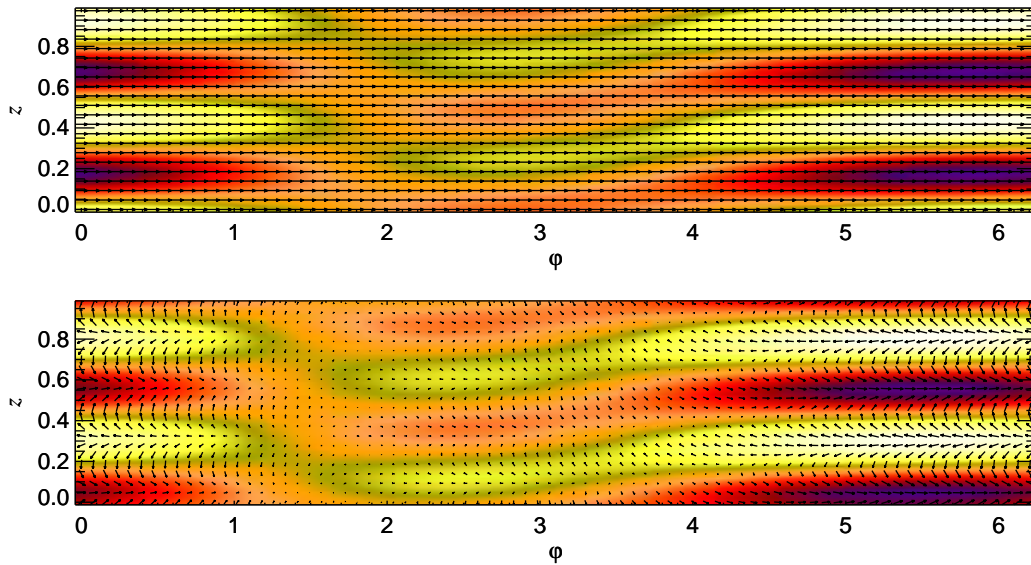


FIGURE 2. Velocity \mathbf{u} (top) and residual magnetic field \mathbf{B}_{res} (bottom) on a cylindrical shell $r = 0.75$ for the linear stage of Run 2a. Representation is as in Fig. 1, in particular bright colours represent positive radial components u_r, B_r .

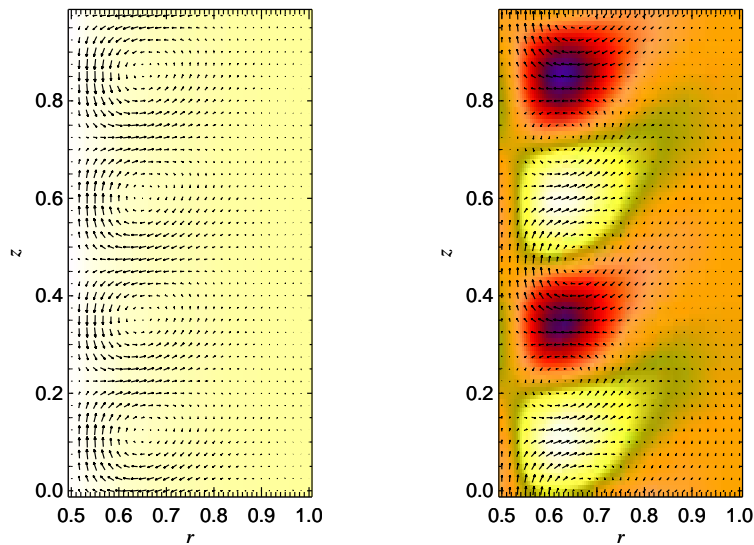


FIGURE 3. As in Fig. 1, but for the linear phase of Run 2a.

The simplest wavy mode can be described as a superposition of modes $(k, m = 0)$ and $(k, m = \pm 1)$ with appropriate phase factors. However, even if some combination of linear modes looks like a wavy mode, this can only be a coincidence, since the relative phases of linear modes are arbitrary, and even evolve in time. Real wavy modes are a nonlinear phenomenon.

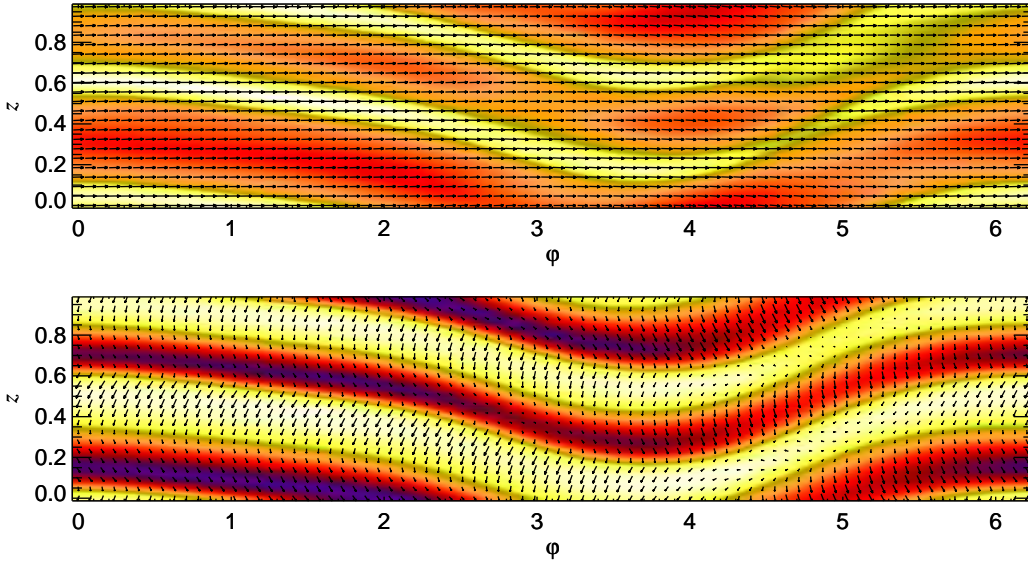


FIGURE 4. Same as Fig. 2, but for the saturated phase of Run 2a.

After some time, the exponential growth of the kinematic phase slows down and eventually a saturated state is reached, in which magnetic and kinetic energy are stationary or vary by a moderate percentage around some average value. This saturated regime can look quite different from the kinematic phase as is shown in Figs. 4 and 5. The azimuthal structure is obviously no longer described by the first three azimuthal modes $|m| = 0, \pm 1$, but involves higher harmonics as well (Fig. 4). This pattern visually resembles the hydrodynamical “wavy mode” of Taylor-Couette flow, although we find here a less symmetric and more structured geometry compared to the simplest manifestations of the hydrodynamical wavy mode.

Not all Runs maintain their geometric structure in the nonlinear regime. As can be seen in Table 1, some Runs (1e and 3a) switch from axisymmetric to non-axisymmetric behaviour when saturating. On the other hand, Run 3a switches from a clear $m = 1$ mode during the linear phase to an axisymmetric saturated state. These findings clearly demonstrate that it can be misleading to extrapolate linear results to the nonlinear regime.

2.3.2. Velocity profile

In Fig. 6, we have plotted u_ϕ as a function of radius for the saturated phase of Run 2a, with three different representations for the azimuthal velocity component: We compare the radial profiles of angular velocity $\omega \equiv u_\phi/r$, azimuthal velocity u_ϕ , and specific angular momentum $l \equiv ru_\phi$. While the boundary values for all three curves are determined by R_1, Ω_1, R_2 , and Ω_2 , the profiles between the boundaries reflect the physics of angular momentum transport. If angular momentum was transported mainly due to radial advection, the profile $l(r)$ would be roughly constant (like entropy is mostly

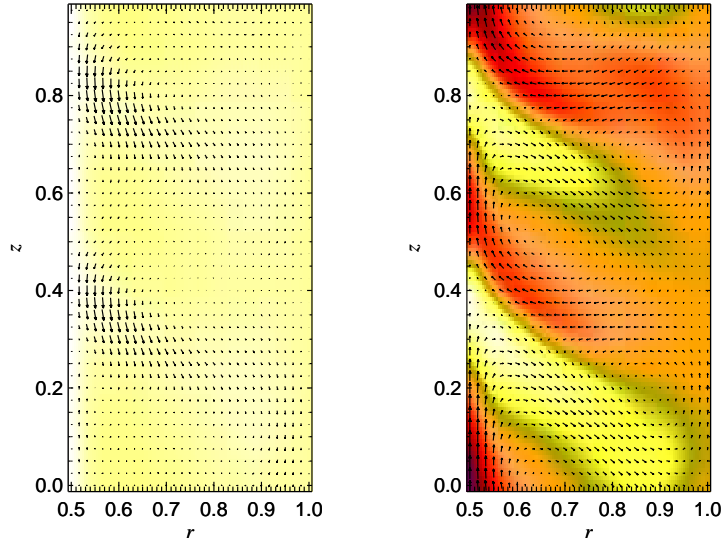


FIGURE 5. Same as in Fig. 3, but for the saturated phase of Run 2a.

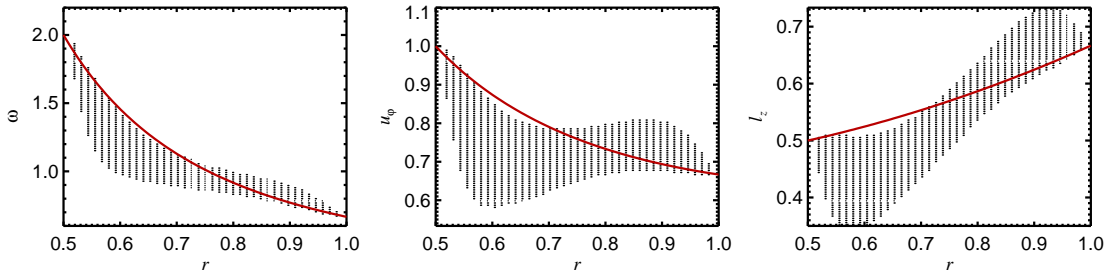


FIGURE 6. Scatter plot showing different representations of the azimuthal velocity component as function of r for the saturated phase of Run 2a. Left: Angular velocity ω . Middle: Azimuthal velocity u_ϕ . Right: Specific angular momentum l_z .

constant in thermal convection layers); this is clearly not the case in Fig. 6. It is rather the angular velocity $\omega(r)$ that has been synchronized by the flow, which is a clear indicator for the magnetic tension force being the dominant mechanism of angular momentum transport.

2.3.3. A potential compressibility effect

For Runs 1a–g, the specific angular momenta on the two cylinders are equal, $l_1 = l_2$, thus we expect the hydrodynamic Couette flow to be marginally stable in the absence of viscosity according to Rayleigh’s criterion. If viscosity is present, it is natural to expect that the system becomes stable because perturbations will now be damped, even if that damping is small. To our surprise, we found however that Run 1a, where the magnetic

field is zero, develops Taylor vortices just like the magnetic cases, albeit the growth rate is lower. This is hard to understand, since l is not only equal on the two cylinders, but according to Eq. (1), we have

$$l(r) = l_1 = \text{const} \quad (10)$$

everywhere. Thus, advection will not have any effect on the distribution of angular momentum, and there is no obvious other mechanism that could transport it at all.

However, compressibility can make a difference. Since we have set *kinematic* viscosity $\nu = \text{const}$, rather than assuming constant *dynamic* viscosity, the r -dependent equilibrium solution is not exactly the Couette profile (1). But any deviation from the Couette profile will introduce a gradient $dl/dr \neq 0$ which takes on both signs (we find that l has a minimum near $r = 0.7$ and thus $dl/dr < 0$ near R_1 and $dl/dr > 0$ closer to R_2). If viscosity is low enough, the part with $dl/dr < 0$ will be unstable and drive Taylor vortices. We thus believe that the flow we find in Run 1a is due to compressibility effects, which cause viscous angular momentum transport.

2.3.4. Helicity and alpha effect

In the context of mean-field theory [30], a crucial parameter describing the magnetic field generation properties of many dynamo systems is the α -effect [31]. In their work on linear properties of magnetic Taylor-Couette flow, Rüdiger & Zhang [27] discussed the possibility of an α -effect in that type of flow. For infinitely long cylinders and in the linear regime, the flow is strictly periodic in z and thus the α effect oscillates around zero along that direction. Noting that such a system has no net α effect, the authors seem to conclude that it is not suitable as a mean-field dynamo.

We note however that it is too restrictive to judge the dynamo properties solely by the net sign of the α -effect. In fact, most cosmic dynamos have almost exactly vanishing $\alpha_{\text{net}} \equiv \int \alpha(\mathbf{x}) dV$, because α is antisymmetric with respect to their equatorial or symmetry plane. Nevertheless the α -effect in these objects is able to generate all kinds of cosmic magnetic fields. It is not a priori clear that a periodic array of cells of alternating kinetic helicity cannot be an interesting dynamo system in its own.

In Figs. 7 and 8, we show the distribution of different quantities related to the α effect. In the quasi-linear approximation, the α effect is given by [32, 33]

$$\alpha = \frac{\tau}{3} \left(-\langle \mathbf{u}' \cdot \text{curl} \mathbf{u}' \rangle + \frac{1}{\rho} \langle \mathbf{B}' \cdot \mathbf{j}' \rangle \right), \quad (11)$$

where τ is the turbulent turnover time and $\mathbf{u}' \equiv \mathbf{u} - \langle \mathbf{u} \rangle$, etc. For our geometry, the averages $\langle \cdot \rangle$ are conveniently taken over azimuth φ . In the figures we show kinetic helicity $H_{\text{kin}} \equiv \langle \mathbf{u}' \cdot \text{curl} \mathbf{u}' \rangle$, the current helicity $H_{\text{cur}} \equiv \langle \mathbf{B}' \cdot \mathbf{j}' \rangle$, their combination (11), and the vertical component of the “turbulent” electromotive force, $\mathcal{E}_z \equiv u'_r B'_\varphi - u'_\varphi B'_r$.

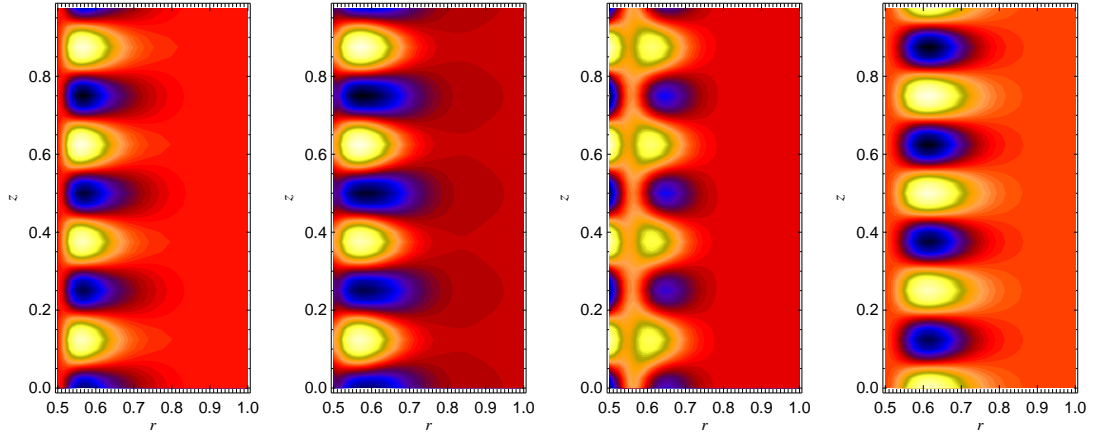


FIGURE 7. Dynamo properties for the linear phase of Run 2a. (a) Kinetic helicity H_{kin} . (b) Current helicity H_{cur} . (c) Alpha effect according to Eq. (11). (d) Vertical component \mathcal{E}_z of fluctuating EMF.

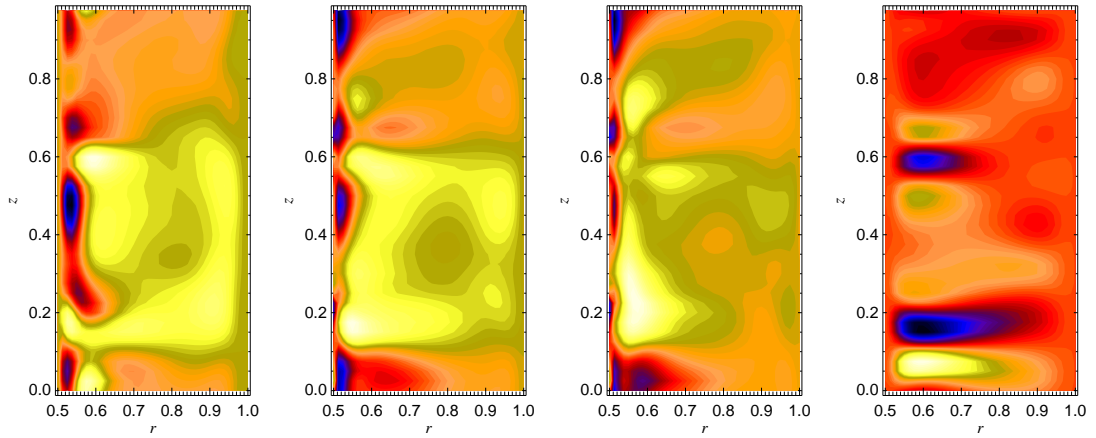


FIGURE 8. As in Fig. 7, but for the saturated stage of Run 2a.

2.3.5. Connection to classical MRI

Finally, in Fig. 9 we show iso-surfaces of angular velocity ω for both, the early nonlinear and the saturated phase. These surfaces approximately also trace the magnetic field lines (which are predominantly vertical). The structure of the iso-surfaces is very reminiscent of the so-called “channel flow” observed in MRI simulations of accretion discs [34], but with a “wavy” φ -dependence superimposed. This once more exemplifies how the MRI in accretion discs and Taylor vortices become one and the same phenomenon in magnetic Taylor–Couette flow.

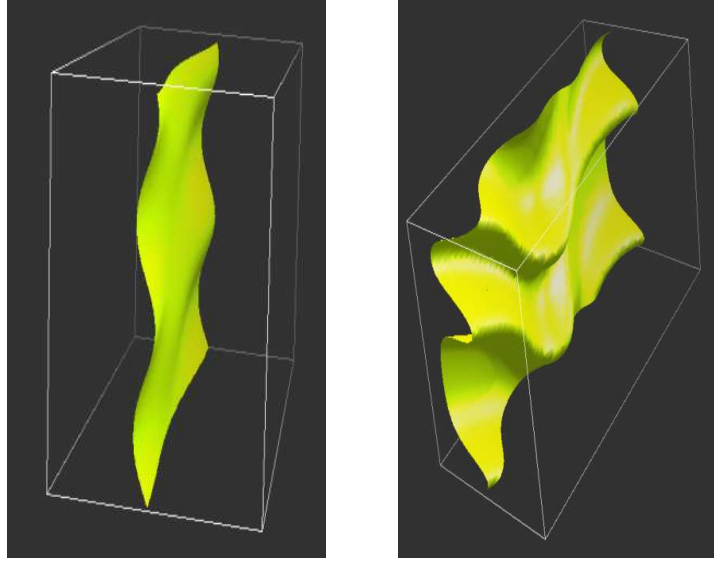


FIGURE 9. Channel flow in the moderately nonlinear case (left) and the saturated case (right).

3. CONCLUSIONS

We have presented a set of numerical simulations of Taylor–Couette flow with an axial magnetic field, and see many indications that for not too low Hartmann numbers the Taylor vortices turn into a manifestation of the MRI.

We have not yet carried out calculations for magnetic Prandtl numbers less than unity, and it would be very interesting to see whether the different geometries of linear and nonlinear evolutions can be found for these more “realistic” parameters as well.

In any case the fact that we can have non-axisymmetric linear modes developing into axisymmetric saturated flows and vice versa should be a clear warning to refrain from extrapolating linear results

REFERENCES

1. Koschmieder, E. L., *Bénard cells and Taylor vortices*, Cambridge Univ. Press, 1993, ISBN 0-521-40204-2.
2. Velikhov, E. P., *Sov. Phys. JETP*, **36**, 1398ff (1959).
3. Chandrasekhar, S., *Hydrodynamic and Hydrodynamic Stability*, Clarendon, Oxford, 1961.
4. Balbus, S. A., and Hawley, J. F., *Astroph. J.*, **376**, 214–222 (1991).
5. Hawley, J. F., and Balbus, S. A., *Astroph. J.*, **376**, 223–233 (1991).
6. Donnelly, R. J., and Ozima, M., *Phys. Rev. Lett.*, **4**, 497–498 (1960).
7. Fleming, T. P., Stone, J. M., and Hawley, J. F., *Astroph. J.*, **530**, 464–477 (2000).
8. Richard, D., and Zahn, J.-P., *Astron. Astrophys.*, **347**, 734–738 (1999).
9. Brandenburg, A., Nordlund, Å., Stein, R. F., and Torkelsson, U., *Astrophys. J.*, **446**, 741–754 (1995).
10. Ziegler, U., and Rüdiger, G., *Astron. Astrophys.*, **356**, 1141–1148 (2000).
11. Hawley, J. F., *Astroph. J.*, **528**, 462–479 (2000).
12. Brandenburg, A., Nordlund, Å., Stein, R. F., and Torkelsson, U., *Astrophys. J.*, **458**, L45–L48 (1996).
13. Mac Low, M.-M., de Avillez, M. A., and Korpi, M. J., “The Turbulent Interstellar Medium: Insights

- and Questions from Numerical Models,” in *How Does the Galaxy Work?*, edited by E. J. Alfaro, E. Pérez, and J. Franco, Kluwer, Dordrecht, 2004.
14. Kitchatinov, L. L., and Rüdiger, G., *Astron. Astrophys.*, **424**, 565–570 (2004).
 15. Laure, P., Chossat, P., and Daviaud, F., “Generation of magnetic field in the Couette–Taylor system,” in *Dynamo and Dynamics, a Mathematical Challenge*, edited by P. Chossat et al., Kluwer, 2001, pp. 17–24.
 16. Willis, A. P., and Barenghi, C. F., *Astron. Astrophys.*, **393**, 339–343 (2002).
 17. Ruzmaikin, A., Sokoloff, D., and Shukurov, A., *J. Fluid Mech.*, **197**, 39–56 (1988).
 18. Gilbert, A. D., *Geophys. Astrophys. Fluid Dyn.*, **44**, 241–258 (1988).
 19. Lupyán, E. A., and Shukurov, A., *Magnetohydrodynamics*, **28**, 234–240 (1992).
 20. Bassom, A. P., and Gilbert, A. D., *J. Fluid Mech.*, **343**, 375–406 (1997).
 21. Ponty, Y., Gilbert, A. D., and Soward, A. M., *J. Fluid Mech.*, **435**, 261–287 (2001).
 22. Ruzmaikin, A. A., Sokolov, D. D., Solov'yov, A. A., and Shukurov, A. M., *Magnetohydrodynamics*, **25**, 6–11 (1989).
 23. Léorat, J., *Magnetohydrodynamics*, **31**, 367–373 (1995).
 24. Gilbert, A. D., and Ponty, Y., *Geophys. Astrophys. Fluid Dyn.*, **93**, 55–95 (2000).
 25. Dobler, W., Shukurov, A., and Brandenburg, A., *Phys. Rev. E*, **65**, 036311–1–13 (2002).
 26. Dobler, W., Frick, P., and Stepanov, R., *Phys. Rev. E*, **67**, 056309–1–10 (2003).
 27. Rüdiger, G., and Zhang, Y., *Astron. Astrophys.*, **378**, 302–308 (2001).
 28. Shalybkov, D. A., Rüdiger, G., and Schultz, M., *Astron. Astrophys.*, **395**, 339–343 (2002).
 29. Willis, A. P., and Barenghi, C. F., *Astron. Astrophys.*, **388**, 688–691 (2002).
 30. Krause, F., and Rädler, K.-H., *Mean-field Magnetohydrodynamics and Dynamo Theory*, Pergamon, 1980.
 31. Steenbeck, M., Krause, F., and Rädler, K.-H., *Z. Naturforsch.*, **21a**, 368–376 (1966).
 32. Pouquet, A., Frisch, U., and Léorat, J., *J. Fluid Mech.*, **77**, 321–354 (1976).
 33. Gruzinov, A. V., and Diamond, P. H., *Phys. Rev. Lett.*, **72**, 1651–1653 (1994).
 34. Hawley, J. F., and Balbus, S. A., *Astroph. J.*, **400**, 595–609 (1992).